nature chemistry

ARTICLES

https://doi.org/10.1038/s41557-020-0465-9

Check for updates

α-Synuclein aggregation nucleates through liquid–liquid phase separation

Soumik Ray[1,6], Nitu Singh[1,6], Rakesh Kumar[1], Komal Patel[1], Satyaprakash Pandey[1], Debalina Datta[1], Jaladhar Mahato[2], Rajlaxmi Panigrahi[1], Ambuja Navalkar[1], Surabhi Mehra[1], Laxmikant Gadhe[1], Debdeep Chatterjee[1], Ajay Singh Sawner[1], Siddhartha Maiti[1], Sandhya Bhatia[3], Juan Atilio Gerez[4], Arindam Chowdhury[2], Ashutosh Kumar[1], Ranjith Padinhateeri[1], Roland Riek[4], G. Krishnamoorthy[5] and Samir K. Maji[1]✉

α-Synuclein (α-Syn) aggregation and amyloid formation is directly linked with Parkinson's disease pathogenesis. However, the early events involved in this process remain unclear. Here, using the in vitro reconstitution and cellular model, we show that liquid–liquid phase separation of α-Syn precedes its aggregation. In particular, in vitro generated α-Syn liquid-like droplets eventually undergo a liquid-to-solid transition and form an amyloid hydrogel that contains oligomers and fibrillar species. Factors known to aggravate α-Syn aggregation, such as low pH, phosphomimetic substitution and familial Parkinson's disease mutations, also promote α-Syn liquid–liquid phase separation and its subsequent maturation. We further demonstrate α-Syn liquid-droplet formation in cells. These cellular α-Syn droplets eventually transform into perinuclear aggresomes, the process regulated by microtubules. This work provides detailed insights into the phase-separation behaviour of natively unstructured α-Syn and its conversion to a disease-associated aggregated state, which is highly relevant in Parkinson's disease pathogenesis.

Liquid–liquid phase separation (LLPS) of biological polymers (protein and RNA) has emerged as a critical phenomenon in the formation of intracellular 'membraneless' organelles[1–7]. Such examples include nucleoli[8], Cajal bodies[9] and promyelocytic leukaemia bodies[2] in the nucleus as well as stress granules in the cytoplasm[10–12]. These liquid condensates concentrate biomolecules (proteins and nucleic acids) at distinct cellular sites to perform various cellular functions[3]. Owing to the lack of physical barriers, the liquid condensates are able to exchange their components rapidly with the surrounding[4,13,14]. Most of the liquid condensates possess common characteristics; for instance, they are highly mobile and spherical in shape, but deform on physical contact, fuse and eventually revert back to the spherical shape[1]. Several proteins known to undergo LLPS contain intrinsically disordered regions that are closely associated with prion-like domains and low-complexity domains (LCDs)[15–17], in which the amino acid variance is extremely low[18]. These intrinsically disordered regions drive LLPS by weak, multivalent interactions between the protein molecules, and thus allow various homotypic and heterotypic interactions of proteins and other biomolecules[10,11,19,20].

Many proteins that initially form highly mobile liquid condensates become more viscoelastic and rigid over time and eventually form a gel-like state that is unable to exchange its component molecules with the surrounding[10,21–23]. This transition could be due to either the entanglement of biopolymers or a stronger association of proteins, which leads to fibril formation, as observed for many proteins, such as FUS[22], TDP-43[24], tau[23,25] and hnRNPA1[10]. In these cases, phase separation might increase the nucleation rate for protein aggregation into amyloid-like fibrils[10,11,17].

α-Synuclein (α-Syn) is a natively unstructured protein[26], and its aggregation into cytotoxic oligomers and amyloid fibrils is associated with Parkinson's disease (PD)[27–29]. Mutations of α-Syn associated with early-onset familial PD[30,31] are known to modulate its aggregation[32], which supports that it has role in PD pathogenesis. Although the mechanism of α-Syn aggregation is an area of extensive research[33–36], the early aggregation events are not well-established. The primary structure of α-Syn consists of three distinct domains: the N-terminal region, an aggregation-prone 'non-amyloid-β component' (NAC) and a flexible C-terminal domain. Although the NAC region primarily drives α-Syn aggregation[37], the majority of familial mutations are at the N terminus, which highlights its importance in α-Syn misfolding and aggregation[38,39].

As α-Syn possesses two LCDs, we hypothesized that it might undergo LLPS under the appropriate conditions. Here we show that, in the presence of a molecular crowder, α-Syn undergoes LLPS, which is further promoted by various PD-associated conditions. We demonstrate that the N terminus and hydrophobic NAC domain majorly drive α-Syn LLPS. Interestingly, our results reveal that α-Syn droplets undergo a liquid to solid-like transition, which leads to a hydrogel formation that contains fibrillar aggregates and oligomers. Further, α-Syn forms liquid droplets even within cells and subsequently transforms into solid-like aggresomes, which is regulated by microtubules. These findings establish that phase separation acts as an initial step towards α-Syn aggregation associated with PD pathology.

Results

LLPS of α-Syn in vitro. To predict α-Syn LLPS, we used the Simple Modular Architecture Research Tool (SMART)[40] and IUPred2[41]

[1]Department of Biosciences and Bioengineering, IIT Bombay, Mumbai, India. [2]Department of Chemistry, IIT Bombay, Mumbai, India. [3]National Center for Biological Sciences, Tata Institute of Fundamental Research, Bengaluru, India. [4]Department of Chemistry and Applied Biosciences, ETH Zurich, Zürich, Switzerland. [5]Department of Biotechnology, Anna University, Chennai, India. [6]These authors contributed equally to this work: Soumik Ray, Nitu Singh. ✉e-mail: samirmaji@iitb.ac.in

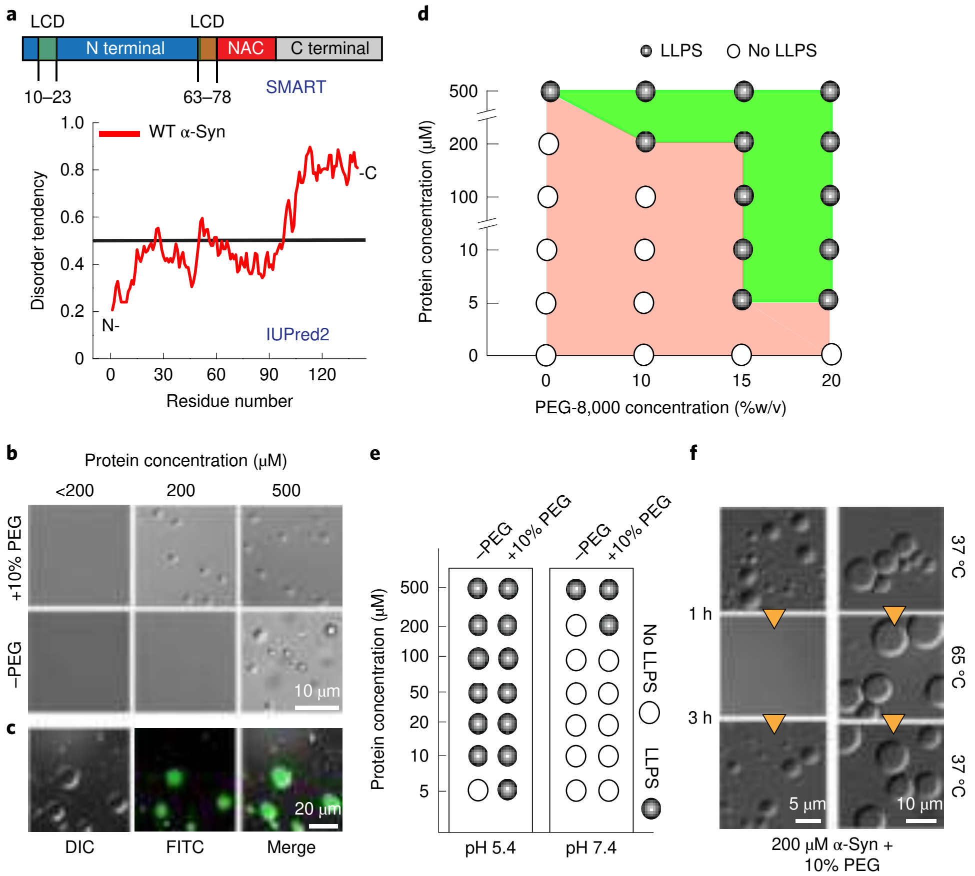

Fig. 1 | α-Syn undergoes LLPS in vitro. a, In silico analysis of the primary sequence of WT α-Syn using SMART (top) to predict the LCDs and IUPred2 (bottom) to analyse the disorder tendency. **b**, Differential interference contrast (DIC) images of α-Syn phase-separated droplets at different protein concentrations in the presence and absence of the molecular crowder PEG-8000 at day 2 (d2). Representative images are shown. **c**, Fluorescence images of FITC-labelled α-Syn (200 μM) phase-separated droplets formed in the presence of 10% PEG-8000 at d15. Representative images are shown. **d**, Regime diagram illustrating the phase separation of α-Syn at different protein and PEG concentrations at d2. **e**, Regime diagram of α-Syn at pH 5.4 and 7.4 ($n=3$ independent experiments). **f**, DIC images of α-Syn (200 μM) droplets in the presence of 10% PEG at d2 (left) and d20 (right) demonstrate the fast and slow reversible nature of the droplets, respectively, on heating (65 °C) and cooling (37 °C). Representative images are shown. All the experiments were performed three times with similar observations (**b-f**).

algorithms to examine the presence of LCDs and intrinsically disordered regions, respectively. SMART analyses predicted two LCDs (residues 10–23 and 63–78, upper panel in Fig. 1a) and IUPred2 revealed disorderness in three segments (residues 26–28, 54–56 and 99–140, lower panel) in the α-Syn sequence. In the presence of a molecular crowder such as 10% polyethylene glycol (PEG)-8000, α-Syn showed the formation of liquid-like droplets in vitro at concentrations ≥200 μM (Fig. 1b and Supplementary Fig. 1). The liquid-droplet formation was further confirmed by light scattering and fluorescence imaging with fluorescein isothiocyanate (FITC)-labelled α-Syn (10% labelled) protein (Fig. 1c and Supplementary Fig. 2). Note that the presence of the 10% labelled protein did not change the major biophysical properties of α-Syn (Supplementary Fig. 3). Further, increasing the molecular crowding decreased the critical concentration of protein for phase separation (Fig. 1d), which suggests that an increased local concentration by molecular crowding is sufficient to initiate α-Syn LLPS.

For developing a phase regime, we compared the phase separation of α-Syn at various concentrations and at different pH values (pH 5.4 and 7.4, in the absence and presence of 10% PEG). At low pH (5.4), α-Syn formed droplets even at 10 μM and 5 μM concentrations in the absence and presence of PEG, respectively (Fig. 1e and Supplementary Fig. 4). As protein phase separation is temperature dependent[19,21,42], α-Syn LLPS was studied at 4, 18, 25 and 37 °C using 200 μM protein. α-Syn formed liquid droplets at all the temperatures (except at 4 °C) after 48 h (Supplementary Fig. 5). To examine the temperature-dependent reversibility, α-Syn droplets (d2) were subjected to a high temperature (65 °C). The droplets initially disappeared after 1 h, but reappeared within 3 h on cooling at 37 °C, which suggests their reversible and liquid-like nature. In contrast, aged (d20) droplets became insensitive to high temperature (65 °C). When heated to 65 °C for 6 h, only the size of the droplets reduced; however, the droplets size completely recovered after 24 h when subsequently incubated at 37 °C (Fig. 1f and Supplementary Fig. 5). This suggests a liquid-to-solid-like transition of α-Syn droplets over time, similar to that of other proteins, which include FUS[22], TDP-43[24] and tau[23].

Dynamics of α-Syn molecules inside liquid droplets. We studied the dynamics of α-Syn molecules in the liquid droplets during their formation and maturation over a period of 20 days. We observed that the size of the droplets increased with time (Fig. 2a) owing to both Ostwald ripening[43] and droplet fusion[44]. For instance, we found the coalescence of two droplets to form a larger-sized droplet (Fig. 2b and Supplementary Video 1), which indicates droplet fusion. Further, the gradual disappearance of the smaller droplets and simultaneous growth of the nearby larger-sized droplets (Supplementary Video 2) suggests the possibility of Ostwald

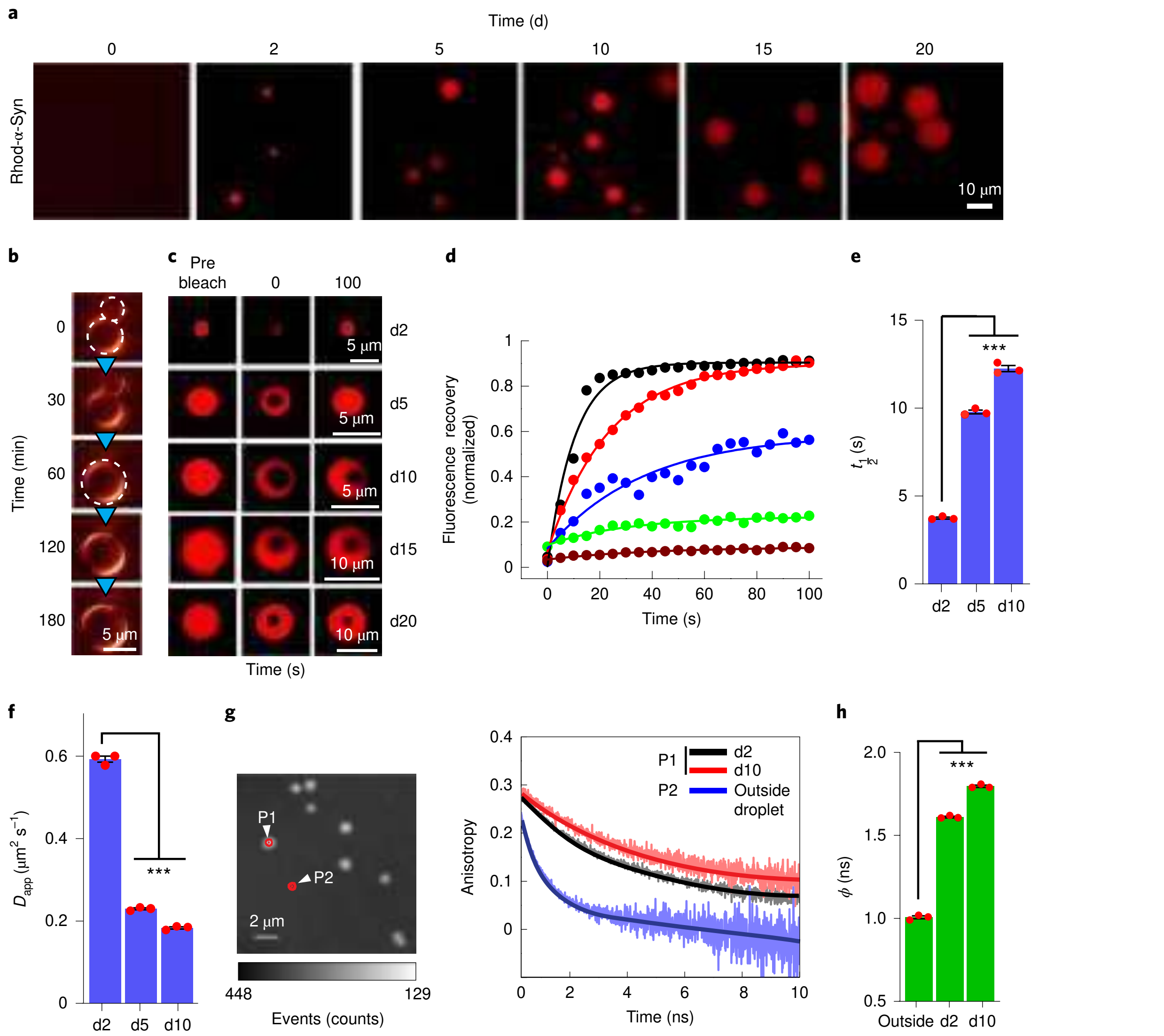

Fig. 2 | The dynamics of α-Syn in LLPS slows down with time. **a**, Fluorescence images showing the growth of NHSrhod-α-Syn droplets over time (NHS, *N*-hydroxysuccinimide). Representative images are shown. **b**, Time-lapse images of an α-Syn droplet showing the fusion of two droplets and the formation of a larger single droplet over the time (represented in 'glow' pseudocolour). Representative results are shown. **c**,**d**, A representative droplet at the indicated time points (**c**) and FRAP measurements of α-Syn droplets at these times to measure the change in dynamics of droplets at d2 (black), d5 (red), d10 (blue), d15 (green) and d20 (brown) (**d**). **e**, $t_{1/2}$ values at the indicated time points. Notably, $t_{1/2}$ could not be calculated for the d15 and d20 droplets due to the negligible recovery after photobleaching. The data represent the mean ± s.e.m. for $n = 3$ independent experiments. Radius of the region of interest = 3 μm. ***$P \leq 0.001$; P values for d5 and d10 were 6.8×10^{-8} and 8.7×10^{-8}, respectively. **f**, D_{app} values at d2, d5 and d10 were calculated from the obtained $t_{1/2}$ and are plotted. The data represent the mean ± s.e.m. for $n = 3$ independent experiments. ***$P \leq 0.001$; P values for d5 and d10 were calculated to be 5.12×10^{-8} and 2.5×10^{-9}, respectively. **g**, Left: representative image of FITC-labelled α-Syn droplets analysed with time-resolved fluorescence anisotropy decay. P1 and P2 are points from inside and outside the droplets, respectively, used for the analysis. Right: fluorescence anisotropy decay curves demonstrating a delayed decay for d10 droplets compared with that for d2 droplets, which indicates the increased rigidity of α-Syn molecules during droplet maturation. All the experiments were carried out with 200 μM protein in the presence of 10% PEG. **h**, ϕ obtained from inside and outside the droplets at d2 and d10 for FITC-α-Syn. The data represent the mean ± s.e.m. for $n = 3$ independent experiments. ***$P \leq 0.001$; P values for d5 and d10 were 2.2×10^{-9} and 4.5×10^{-9}, respectively. For **e**, **f** and **h**, the statistical significance was calculated using one-way analysis of variance (ANOVA) followed by a Student–Newman–Keuls post hoc test with a 95% confidence interval. All the experiments were performed three times with similar results (**a**–**d**,**g**).

ripening[43]. To characterize the dynamics of the proteins inside liquid droplets, we performed fluorescence recovery after photobleaching (FRAP) experiments using droplets formed by rhodamine-labelled α-Syn (rhod-α-Syn) (10% labelled). Similar to FITC, the presence of 10% rhodamine-labelled protein did not alter any biophysical properties of α-Syn (Supplementary Fig. 3). Immediately after droplet formation (d2), FRAP studies revealed a rapid (Half-life ($t_{1/2}$) of 3.75 s) and complete fluorescence recovery (~96%). The kinetics and % recovery, however, decreased substantially with time (~7.5% recovery at d20) (Fig. 2c–e). From the $t_{1/2}$, we estimated the apparent diffusion coefficient (D_{app}) of the protein molecules to be 0.584, 0.23 and 0.18 μm² s⁻¹ for d2, d5 and d10, respectively (Fig. 2f). The decrease in FRAP recovery (on ageing) indicates a change in the material properties (such as rigidity) that are probably due to the aggregation of proteins inside the droplets[10,22,23]. The decreased molecular diffusion of α-Syn inside the droplets during maturation might be attributed to a change in the viscoelasticity of the droplets[8,23].

Although FRAP measurements provided information on the translational dynamics of α-Syn in liquid droplets, we performed microscopy-based time-resolved fluorescence anisotropy decay to reveal rotational dynamics (both at local and global levels)[45] of α-Syn. We measured the anisotropy decay from inside (P1) and outside (P2) FITC-tagged α-Syn droplets at different time intervals (Fig. 2g). The data clearly showed a reduced rotational motion and therefore more rigidity (rotational correlation times (ϕ) = 1.6 ns at d2) of the protein molecules inside the droplet compared with those outside (ϕ = 1.0 ns) (Fig. 2h and Supplementary Table 1). However, unlike the decay pattern obtained from outside the droplets, the anisotropy decays from inside them showed a y intercept of the asymptote. This reflects the amplitude of a very long correlation time (C) that exists due to the higher rigidity of the molecules[46]. Furthermore, α-Syn molecules inside the d10 droplets were more rigid (ϕ = 1.8 ns) than the freshly formed d2 droplets (ϕ = 1.6 ns). These observations, along with the FRAP recovery data, clearly point to a liquid-to-solid-like transition of α-Syn on ageing.

PD-associated factors and familial mutations accelerate α-Syn LLPS and aggregation. PD is mostly a sporadic disorder in which environmental and cellular factors play a major role in the disease pathogenesis[47]. Factors such as metal ions[48], interaction with lipid membranes[49], Ser129 phosphorylation[50] and familial mutations[32] are known to play critical roles in α-Syn aggregation in PD pathogenesis[51]. For a possible correlation between phase separation and aggregation, we monitored LLPS and aggregation kinetics of α-Syn in the presence and absence of metal ions (Cu^{2+} and Fe^{3+}), liposomes, phosphomimetic S129E and the most characterized familial mutants A53T[30] and E46K[31]. As controls, we also monitored LLPS and aggregation by wild-type (WT) α-Syn alone (without PEG) and in the presence of dopamine, a known inhibitor of α-Syn fibril formation[52]. PD-promoting factors accelerated α-Syn aggregation, as evident by a thioflavin T (ThT) fluorescence assay (Fig. 3a) and their corresponding reduced lag times (Extended Data Fig. 1). Furthermore, the aggregated state showed amyloid-like fibrils as confirmed by transmission electron microscopy (TEM). In contrast, dopamine delayed the aggregation and α-Syn alone did not show any aggregation even after 30 days of incubation (Fig. 3a). Importantly, when we analysed LLPS in identical experimental conditions, we found that Cu^{2+}, Fe^{3+} and liposomes accelerated the liquid-droplet formation (~24 h) even in the absence of PEG (Fig. 3b). Further, the S129E phosphomimetic α-Syn phase separated at a faster rate in the presence of ≥1% PEG compared with WT under identical conditions (Extended Data Fig. 1). Apart from faster rate of liquid-droplet formation, many of these factors also reduced the critical concentration required for LLPS (Extended Data Fig. 1). For instance, α-Syn formed liquid droplets at a 5 μM concentration in the presence of 100 μM Cu^{2+} or 1 mM liposomes. This suggests that elevated levels of these factors increased the intermolecular interaction of α-Syn molecules[49,53,54] and therefore, lowered its critical concentration for phase separation. Similarly, two familial mutants, A53T[30] and E46K[31], showed faster aggregation than WT α-Syn in vitro (Fig. 3a) and phase separated in the presence of PEG after 48 h and 24 h, respectively (Fig. 3b). In contrast, we did not observe LLPS of WT α-Syn (with 10% PEG) in the presence of dopamine until d20, which was also confirmed by TEM analysis (Extended Data Fig. 1). Moreover, these droplets did not grow in size even after one month of incubation, which suggests a very slow rate of maturation.

FRAP analysis of droplets formed in the presence and absence of PD factors showed similar % fluorescence recoveries (except for Cu^{2+} and Fe^{3+}), but with significantly reduced recovery rates (higher $t_{1/2}$ and lower D_{app}) (Fig. 3c,d and Extended Data Fig. 1). This suggests that the translational dynamics of the molecules in the droplets is slower in the presence of these PD-associated factors, which might eventually cause an enhanced aggregation and lead to early maturation of the droplets. The microscopy-based time-resolved anisotropy decay measurements of α-Syn droplets showed a much slower anisotropy decay kinetics (increased ϕ and %C) in the presence of the PD-associated factors compared with the droplets formed in the absence of these factors (Fig. 3e–g and Supplementary Table 1). This further supports that the rigidity of the molecules inside the droplets formed in the presence of PD-associated factors is higher than that in α-Syn droplets formed in the presence of PEG.

Aggregation state of α-Syn during LLPS and liquid-to-solid transition. To establish a direct correlation between α-Syn aggregation (the formation of oligomers and fibrils) and LLPS, we simultaneously monitored the aggregation kinetics using ThT fluorescence and LLPS using various microscopic techniques. Moreover, during LLPS and aggregation, we isolated and quantified the relative amounts of different α-Syn species formed over time (from the same sample) (Fig. 4a and Supplementary Fig. 6). A similar method was used previously for the isolation of oligomeric intermediates of α-Syn[55,56]. The isolated species were characterized for their secondary structure using circular dichroism and morphology by TEM (Supplementary Fig. 7). The aggregation kinetics and LLPS showed that the liquid droplets formed in the early lag phase of aggregation (Fig. 4b(inset),c). The quantification of different species showed ~90% of low molecular weight (LMW) α-Syn (majorly monomeric)[55,57], small amounts of oligomers (~8%) and fibrils (~2%) at the early stages (d5) of LLPS (Fig. 4b). However, a substantial decrease in the LMW population and concomitant increase in fibrils was observed during the maturation of the droplets. Note that the amount of oligomers remained unchanged from d10 to d30 (Fig. 4b), which suggests that the oligomeric intermediate might have reached a 'steady state' (according to steady-state approximation)[58]. The TEM and circular dichroism data showed that LMW fractions are mostly amorphous with a random coil structure. The oligomeric fractions showed mostly a globular morphology with a helical structure (except at d5 and d10). The fibrillar fractions contain predominately amyloid fibrils with a β-sheet structure; however, a random coil component was also observed on d5 (Supplementary Fig. 7). Although a helix-rich structure is known for tetrameric[59] and membrane-bound monomeric α-Syn[26], oligomeric helix-rich structures are also evident during α-Syn aggregation[55]. Collectively, these data clearly point to a dynamic interplay between various α-Syn species (monomer, oligomers and fibril) in which the monomer gradually converts into fibrillar aggregates via an oligomer-mediated process during LLPS.

Further, we also microscopically examined the liquid droplets at various time intervals during the entire process of LLPS and aggregation (30 days). Thioflavin S (ThioS) staining of WT α-Syn showed a diffused fluorescence signal in the background at the beginning of phase separation; however, at later stages (d5 onwards), ThioS readily co-partitioned into the droplets, which demonstrates the presence of amyloid-like aggregates. This was further confirmed by TEM imaging, which showed fibrillar aggregates at d30 (Fig. 4c). Interestingly, after d20, we observed protein aggregates emerging from the subset of droplets (Fig. 4d) and fibril-like structure was observed inside individual droplets when imaged using high-resolution TEM (Fig. 4e). After d30, the LLPS-solution transformed into hydrogel as confirmed by gel-inversion test and scanning electron microscopy (SEM) (Fig. 4f). The frequency sweep bulk rheology measurement with α-Syn hydrogel revealed higher storage modulus (surface elasticity, G′) over loss modulus (surface viscosity, G′′) suggesting gel and/or solid-like behaviour (Fig. 4g).

Next, we asked how the two familial mutations, A53T and E46K, modulate the liquid-to-solid transition and gel formation of α-Syn. Apart from increased number, larger-sized droplet formation and

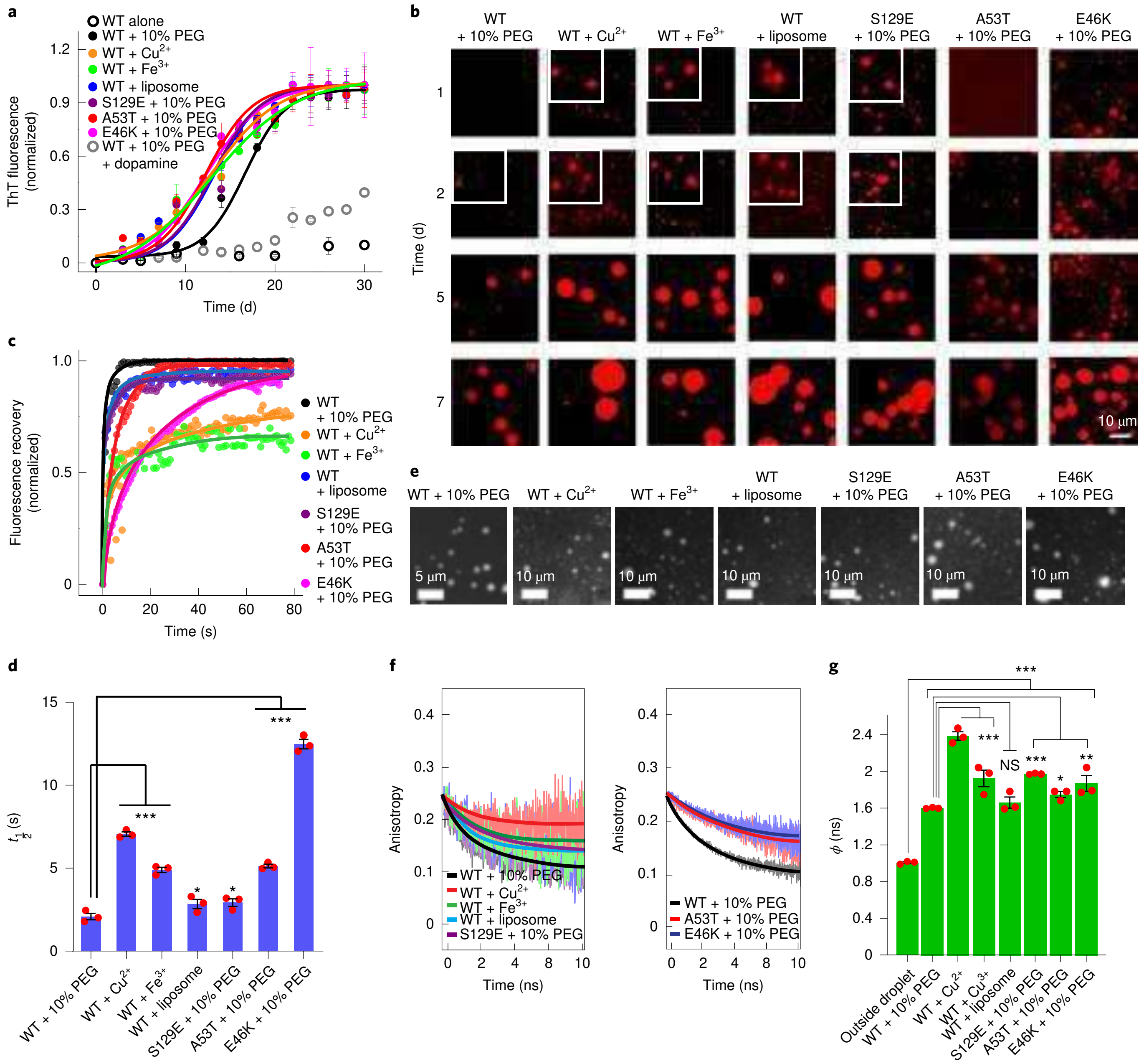

Fig. 3 | PD-associated aggregation factors promote α-Syn LLPS. a, ThT-fluorescence assay demonstrating α-Syn aggregation kinetics under non-rotating (static) conditions in the presence of various factors (PEG, Cu^{2+}, Fe^{3+}, liposomes, S129E-phosphomimetic, A53T and E46K mutations, and dopamine). WT α-Syn (200 μM) was incubated with 10% PEG, 50 μM Cu^{2+}, 50 μM Fe^{3+}, 1 mM liposomes and 200 μM dopamine (with 10% PEG). At the same time, 200 μM S129E, A53T and E46K α-Syn were incubated with 10% PEG for the LLPS study. WT α-Syn alone was taken as a control. The data represent the mean ± s.e.m. for $n=3$ independent experiments. **b**, Representative fluorescence microscopic images of rhod-α-Syn droplets formed in the presence of PD-associated factors at the indicated time points. The formation of liquid droplets occurs within 24 h in the presence of the aggregation accelerating factors, whereas in the presence of PEG, the time taken is ~48 h. **c**,**d**, The dynamics of α-Syn molecules inside the droplets measured using FRAP. The normalized FRAP curves of α-Syn droplets at d2 (**c**) and the corresponding $t_{1/2}$ (**d**). The data represent the mean ± s.e.m. for $n=3$ independent experiments. Radius of the region of interest = 2 μm. $^{***}P \leq 0.001$, $^{*}P \leq 0.05$. The P values for WT + Cu^{2+} ($^{***}P = 5.8 \times 10^{-4}$), WT + Fe^{3+} ($^{***}P = 9.3 \times 10^{-7}$), WT + liposome ($^{*}P = 0.04$), S129E + PEG ($^{*}P = 0.05$), A53T + PEG ($^{***}P = 3.5 \times 10^{-7}$) and E46K + PEG ($^{***}P = 2.5 \times 10^{-12}$) were calculated with respect to WT + PEG. **e**,**f**, Time-resolved fluorescence anisotropy decay curves obtained from inside the phase-separated droplets of FITC-labelled WT α-Syn formed in the presence of various PD-associated factors and two familial mutations (A53T and E46K). **e**, Reference fluorescence images of the droplets formed under various conditions from which the time-resolved anisotropy data points were collected. **f**, Time-resolved anisotropy decay curves obtained from the inside of the droplets (shown in **e**) under given conditions at d2. $n=3$ independent experiments. **g**, Bar plot showing ϕ of the droplets at d2; the data represent mean ± s.e.m. for $n=3$ independent experiments. The P values for all the samples were calculated to be $^{***}P < 0.001$ compared with outside the droplet; P values for WT + Cu^{2+} ($^{***}P = 7.5 \times 10^{-7}$), WT + Fe^{3+} ($^{***}P = 9.6 \times 10^{-4}$), WT + liposome (not significant (NS), $P > 0.99$), S129E + PEG ($^{***}P = 0.001$), A53T + PEG ($^{*}P = 0.03$) and E46K + PEG ($^{**}P = 2.2 \times 10^{-3}$) were calculated with respect to WT + PEG. Statistical significance was determined using one-way ANOVA followed by a Student–Newman–Keuls post hoc test with a 95% confidence interval (**d**,**g**). All the experiments were performed three times with similar observations.

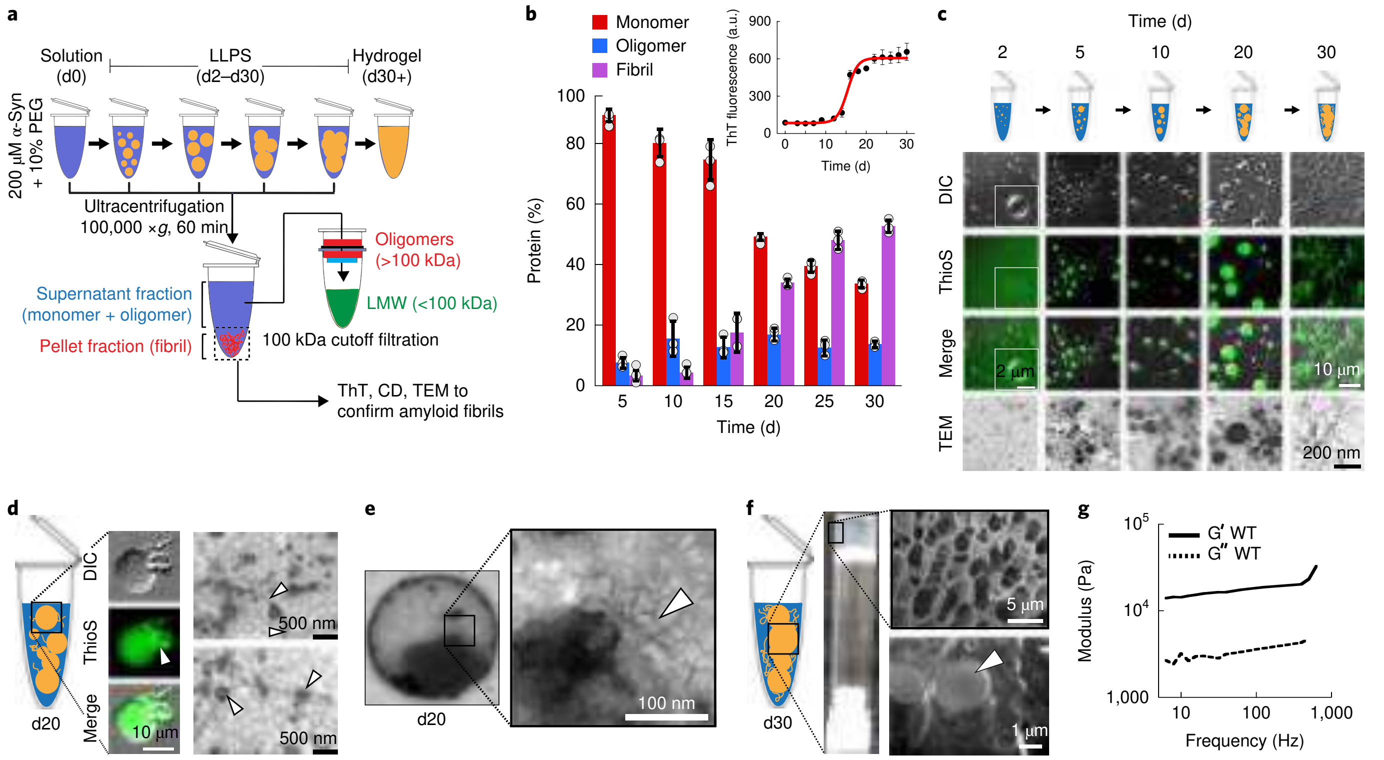

Fig. 4 | α-Syn phase-separated droplets mature and age into fibrillar aggregates. a, Schematic showing the isolation of different α-Syn species (200 μM) and their quantification during LLPS and aggregation. **b**, Isolation of α-Syn species during aggregation and LLPS. α-Syn in the presence of 10% PEG was incubated without agitation at 37 °C for LLPS or aggregation. At various time points, aliquots were taken to isolate the monomers, oligomers and fibrils. In parallel, a ThT fluorescence assay was performed to monitor the aggregation and amyloid formation by α-Syn. During LLPS and aggregation, the relative percentage of the monomers (LMW), oligomers and fibrils at the indicated time points were quantified and plotted. The data represent mean ± s.e.m. for $n=3$ independent experiments. Inset: aggregation kinetics for WT α-Syn under LLPS conditions monitored by the ThT assay. The data represent mean ± s.e.m. for $n=3$ independent experiments. **c**, Time-dependent changes of α-Syn liquid droplets analysed by DIC imaging, ThioS staining, fluorescence microscopy and TEM imaging. At d2, α-Syn droplets show no ThioS co-partitioning, possibly due to the lack of ThioS-positive aggregates. At later time points, ThioS readily co-partitions inside the droplets, which highlights aggregation during the maturation of droplets. At the end of the incubation period (after d30), the coverslip shows ThioS-positive mesh-like structures. **d**, Appearance of fibrils at d20 of the droplet incubation at 37 °C. ThioS staining and TEM images show the presence of protein aggregates (white arrows) adjacent to the droplets. **e**, Magnified TEM image showing the presence of fibril-like structures inside a droplet (white arrow). **f**, Gel formation confirmed by a gel inversion test after d30 by α-Syn in the presence of 10% PEG at 37 °C. The SEM images show the presence of liquid droplets embedded in the hydrogel bed (white arrow). **g**, Bulk rheology measurement of a LLPS sample after d30 showing a higher storage modulus (G') than the loss modulus (G''), which confirms its gel state. $n=2$ independent experiments. All the experiments described in **c**–**f** were performed three times with similar observations.

higher light scattering, both the mutants showed a faster aggregation (Extended Data Fig. 2). Moreover, ThioS co-partitioned early for the A53T and E46K droplets (at d2) compared with WT α-Syn co-partitioning, which suggests a faster aggregation of A53T and E46K into amyloid fibrils inside the droplets. Both mutants also showed a stiffer hydrogel formation compared with that of WT protein (Extended Data Fig. 2).

Domain interactions responsible for α-Syn LLPS. To determine the domain interactions responsible for LLPS at the residue-specific level, two-dimensional [^{15}N–^{1}H] heteronuclear single quantum coherence (HSQC) spectra were recorded. We chose WT α-Syn along with two familial mutants (A53T and E46K) to compare the extent of domain interactions. The narrow signal dispersion in the direct dimension (H^N) indicated the disordered state of the proteins. During LLPS, WT α-Syn showed a gradual decrease in the intensities of the residues at the N terminus (V3-A27, V37-K43 and H50-E57) and NAC region (V74-V82 and A89-K97). The residues in the C terminus (I112–N122) showed a comparatively lower reduction in intensity (Fig. 5a,b and Supplementary Fig. 8). Similar observations were also seen for both A53T and E46K; however, with a rapid decrease in the NMR signal at the N terminus and NAC regions (Supplementary Figs. 9 and 10). For E46K, after d3, amide cross-peaks of most of the residues disappeared while new peaks appeared, which indicates major changes in the conformation. At d20, extensive broadening and shifting of the NMR signal suggested a higher-order structure formation by all three proteins. The NMR data therefore suggest that, apart from the disordered N terminus, the hydrophobic NAC region might also be involved in α-Syn LLPS. This inference is further supported by time-resolved fluorescence decay measurements with site-specific single Trp-mutants of α-Syn (N terminal, 3W; NAC region, 71W; C terminal, 124W and 140W). Previously, it was shown that introduction of Trp at these positions did not alter the properties of α-Syn[60]. The time-resolved fluorescence intensity decay analysis suggests that there is no substantial change in the local environment of the Trp probes due to LLPS (Fig. 5c,d). However, the structural rigidity of the N terminus and the NAC region is considerably higher compared with that of the C terminus, as evident from the faster correlation time (ϕ_1) and its amplitude (α_1) (Fig. 5e,f and Supplementary Fig. 11) after LLPS.

To examine whether the structural rigidity at the N terminus and the NAC region is due to the intermolecular interactions after phase

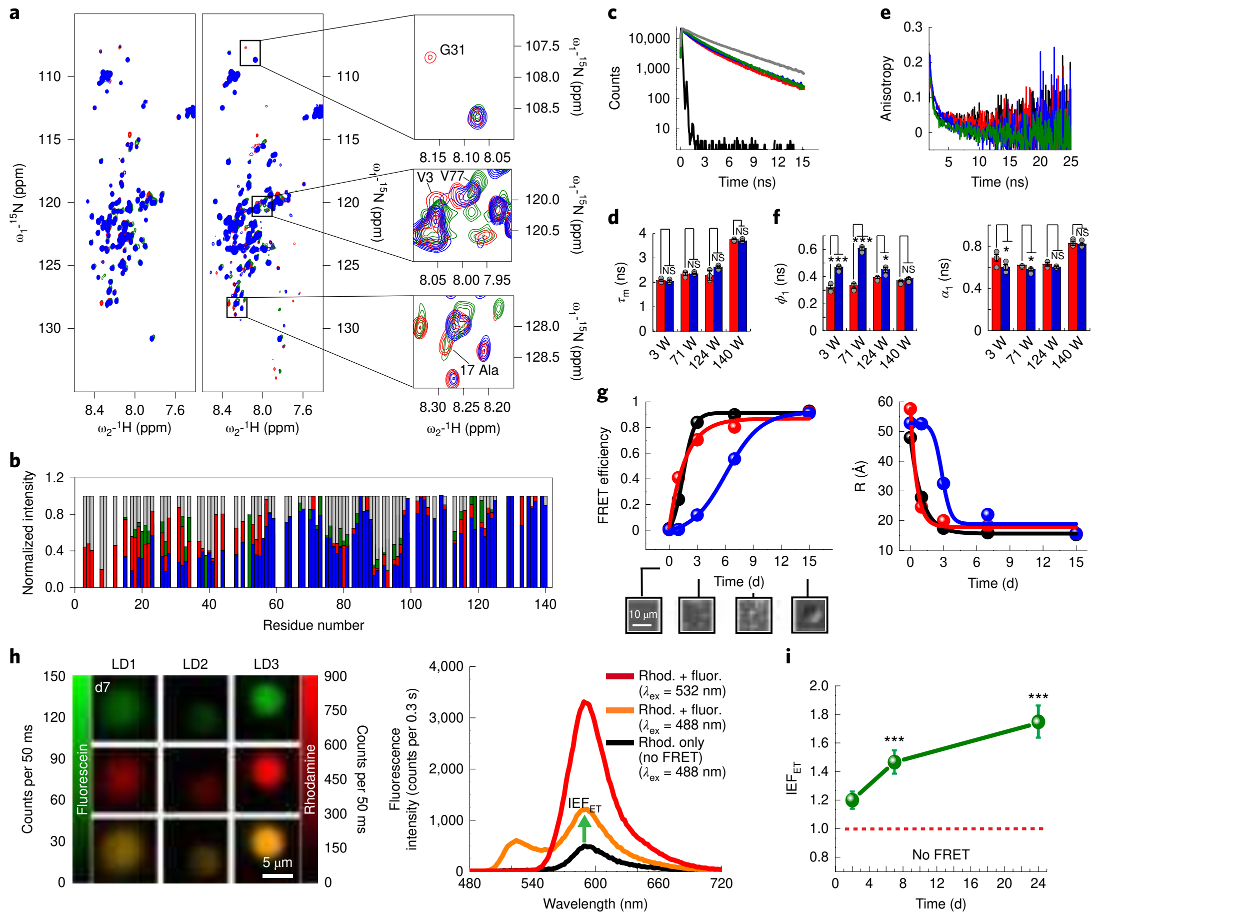

Fig. 5 | Site-specific conformational changes and dynamics of α-Syn during LLPS. a, Overlapped [^{15}N–^{1}H] HSQC spectra of WT α-Syn (red), A53T (blue) and E46K (green) on d0 (left) and d2 (right) showing the residues (G31, V3 and V17, enlarged areas) of WT and mutants have substantial differences in their intensities post-LLPS. n=2 independent experiments. **b**, Normalized intensity (I/I_0) profile of amide cross-peaks from ^{1}H–^{15}N HSQC spectra of WT (red), A53T (blue) and E46K (green) on d2 (post-LLPS) showing a substantial decrease in intensities for residues at the N terminus and NAC domain after LLPS (d0, grey). The extent of the intensity decrease is greater for A53T and E46K compared with that for WT. n = 2 independent experiments. **c**, Time-resolved fluorescence intensity decay of α-Syn Trp substitution mutants (positions 3W (red), 71W (blue), 124W (green) and 140W (grey)) on d2 after phase separation; black line, intensity of reflectance. n = 3 independent experiments. **d**, The mean lifetime (τ_m) computed from time-resolved fluorescence data before (d1, red bars) and after (d2, blue bars) the phase separation event showing no significant difference. The data represent mean ± s.e.m. for n = 3 independent experiments. The P values (*P > 0.05) were determined using a two-tailed paired Student t-test with a 95% confidence interval. The calculated P values for 3W, 71W, 124W and 140W were NS P = 0.53, NS P = 0.81, NS P = 0.14 and NS P = 0.85, respectively. **e**, The time-resolved fluorescence anisotropy decay of α-Syn Trp substitution mutants (positions 3W (black), 71W (red), 124W (blue) and 140W (green)) after phase separation (at d2). n=3 independent experiments. **f**, The fluorescence anisotropy decay analysis reflects a higher rigidity at the N terminus (3W) and the NAC region (71W) compared with that at the C terminus (red, soluble; blue, phase separation (d2)). The magnitude of the first correlation time (ϕ_1) is higher for 3W and 71W Trp (left), whereas the corresponding amplitudes (α_1) are lower (right). n = 3 independent experiments. The P values (*$P \leq 0.05$, **$P \leq 0.005$, ***$P \leq 0.001$ and NS P > 0.05) were determined using a two-tailed paired Student t-test with a 95% confidence interval. The P values for 3W, 71W, 124W and 140W were ***P = 0.001, ***$P = 9 \times 10^{-4}$, NS P = 0.05 and NS P = 0.10, respectively (left), and *P = 0.05, *P = 0.05, NS P = 0.54 and NS P = 0.71 (right), respectively. **g**, Left: spectroscopy-based FRET analysis of the bulk system that involves a Trp–Cys DTNB intermolecular FRET pair. The FRET efficiencies for the N-terminal region (3W–3C (DTNB), black line) and the NAC domain (71W–74C (DTNB), red line) were higher from the beginning of the LLPS compared with that of the C terminus (124W–124C (DTNB), blue line) region, which showed a higher extent of FRET during the later stage. Images below the x axis are representative DIC microscopy images of droplets obtained from the sample at indicated time-points. Right: the intermolecular distance (R) calculated from the FRET efficiency values are plotted against time with the R_0 value considered as 23 Å. The experiments were repeated twice with similar results. **h**, Left: single-droplet fluorescence imaging of droplets that contain fluorescein (donor) and rhodamine (acceptor) as the intermolecular FRET pairs for the 74th position (NAC). LD, liquid droplet. Right: the red and orange lines show the emission spectra from a droplet excited at 532 nm and 488 nm, respectively. Note, the rhodamine emission at the 488 nm excitation shows an enhanced emission compared with the transfer scenario without energy (black line) from the same droplet, which indicates the closeness of the two fluorophores after LLPS. The experiment was repeated three times with similar results. Rhod., rhodamine; fluor., fluorescein. **i**, The evolution of the energy transfer at the 74th position due to intermolecular FRET shows that the NAC regions of α-Syn draw close to each other with time during the aggregation inside the droplets. The data represent mean ± s.e.m. for n = 3 independent experiments. The P values (***$P \leq 0.001$) were determined using a one-way ANOVA followed by a Student–Newman–Keuls post hoc test with a 95% confidence interval. The calculated P values for d7 and d24 (with respect to d2) were ***$P = 5 \times 10^{-9}$ and 1.2×10^{-11}, respectively.

separation, we performed Förster resonance energy transfer (FRET) experiments. We used single cysteine (Cys) mutants of α-Syn (3C, 74C and 124C) labelled with 5-5′-dithio-bis-(2-nitrobenzoic acid) (DTNB) as acceptors and complimentary Trp mutants as donors[61]. The energy transfer efficiency for the C terminus (124W–124C) at the early stages of LLPS, however, was low compared with those of the N-terminal and NAC regions (Fig. 5g and Supplementary Figs. 12 and 13). This suggests that the interdomain interaction of the N-terminus and NAC regions might drive the α-Syn droplet formation.

To further establish the involvement of these domains within the droplets as they mature into more solid-like phases, we performed FRET microscopy for the α-Syn NAC domain at a single-droplet resolution. We chose fluorescein-5-maleimide-labelled α-Syn at the 74th position as the donor and rhodamine-C2-maleimide-labelled α-Syn at the same position to be the acceptor. Using these, three phase-separated samples were prepared that comprised only donors (fluorescein-α-Syn), only acceptors (rhodamine-α-Syn) and an equimolar ratio of donors and acceptors.

Energy-mapped and spatially resolved fluorescence imaging of individual liquid droplets that contained both donor and acceptor reveal an enhanced sensitized emission of the acceptor fluorophore when the donor fluorophore was selectively excited (Fig. 5h). This served as a signature of intermolecular FRET owing to proximity of a significant fraction of donor- and acceptor-labelled proteins. Further, in each droplet, the extent of enhancement (intensity enhancement factor due to energy transfer, IEF_{ET}) in the sensitized emission (or the apparent FRET efficiency (Supplementary Methods)) gradually increased with incubation time (Fig. 5i, Supplementary Fig. 14 and Extended Data Fig. 3), which indicates a progressively closer proximity of the α-Syn molecules within each droplet.

The importance of the α-Syn NAC domain in LLPS is further evident because β-synuclein, which lacks the eight hydrophobic amino acid stretch in the NAC domain, neither showed aggregation, as previously shown[62], nor LLPS under the experimental conditions (Extended Data Fig. 4). Interestingly, in LLPS-relevant conditions, another human synuclein family protein, γ-synuclein also did not show any phase separation and/or aggregation, even on extended incubation (Extended Data Fig. 4). γ-Synuclein is known to aggregate very slowly[55], which might be due to the absence of two Tyr residues at the C terminus and the substitution of three glycines in the NAC domain with highly charged glutamate residues. In contrast, the α-Syn core (30–110 residues)[63] exhibits both a faster aggregation and LLPS compared with the WT α-Syn (Extended Data Fig. 4), which provides further evidence that the core/NAC domain is essential for LLPS.

LLPS and liquid-to-solid transition of α-Syn in mammalian cells. To demonstrate α-Syn LLPS in cells, we cultured HeLa cells that overexpressed tetracysteine-tagged α-Syn (C4-α-Syn) for 24 and 48 h and subsequently stained C4-α-Syn with FlAsH-EDT_2 (fluorescein arsenical hairpin binder). Only ~20% of the cells showed cytoplasmic protein accumulates, whereas the remaining cells showed a diffused pan-cellular localization of C4-α-Syn (Fig. 6a). Based on the possible pathological link between iron and α-Syn[64,65], we examined the effect of iron on α-Syn LLPS in cells. Strikingly, after 24 h of treatment with 10 mM ferric ammonium citrate, >95% of the cells displayed cytoplasmic droplet-like assemblies (285 ± 116 droplets per cell) (Fig. 6a and Extended Data Fig. 5) with a spherical shape of average diameter 0.46 μm (Fig. 6b and Supplementary Video 3). After 48 h, these droplets were largely clustered and localized at the perinuclear region (Supplementary Video 5). However, the number of droplets decreased considerably after 48 h (76 ± 21 droplets per cell) with an increase in their average diameter to 0.61 μm (Fig. 6b). The 24 h droplets were highly mobile and underwent frequent fusion events with a rapid relaxation into spherical assemblies (Fig. 6c), indicative of their liquid-like state. These droplets did not show any colocalization with Nile red (stain for lipid droplets)[66] and markers for membrane-bound organelles (lysosomes and mitochondria) (Extended Data Fig. 5), which suggests their membraneless state.

To examine the dynamic properties of C4-α-Syn molecules, we performed in-cell FRAP. As a control, the region with a diffused expression was chosen to determine the intracellular dynamics of the FlAsH-stained C4-α-Syn. We found a partial recovery (~56% recovery at $t_{1/2} = 10 \pm 3.04$ s) of the droplet-free region, which suggests that C4-α-Syn diffuses slowly in the cellular milieu (data not shown). After 24 h of treatment, the fluorescence recovery within the droplets was faster ($t_{1/2} = 5.4 \pm 2.33$ s) compared with that at 48 h ($t_{1/2} = 23 \pm 7.6$ s). This indicates that the α-Syn molecules at 24 h can diffuse and equilibrate with the cytoplasmic pool, in agreement with the properties of the liquid-like state (Fig. 6d). The decreased dynamics at 48 h can be attributed to the liquid-to-solid-like transition, which might be due to the aggregation of C4-α-Syn within these droplets. A similar droplet formation and liquid-to-solid transition was also observed when cells were treated with another metal ion, Cu^{2+} (Extended Data Fig. 5). However, the maturation of the copper-induced droplets was faster (36 h) compared with that of the iron-induced droplets (48 h), which is in accordance with in vitro FRAP and anisotropy studies (Fig. 3).

Subsequently, we performed single-particle tracking measurements inside cells to investigate the diffusion dynamics of individual α-Syn droplets after 24 and 48 h. Statistical analysis of the single-particle-tracking data after 24 h revealed a predominantly super-diffusive behaviour (exponent, $\alpha > 1$) of the droplets, which indicates an active or facilitated motion of the droplets, probably assisted by the cellular machinery (Fig. 6e and Supplementary Fig. 15). The calculated straightness of the particle tracks also showed a positive correlation with their α values, which further supports the directed motion of these liquid-like droplets. However, after 48 h, the α distribution shifted to lower values ($\alpha \leq 1$) for the majority of droplets (Fig. 6e), indicating a (sub)diffusive behaviour, which might be governed by the droplet size and its microenvironment.

To probe the mechanism of super-diffusive displacement of α-Syn droplets and the possible involvement of microtubules, cells were treated with the microtubule-depolymerizing agent nocodazole. On microtubule destabilization, the majority of the droplets formed at 24 h clumped together (Fig. 6f and Supplementary Video 4). The calculated α-distribution after the microtubule destabilization showed a considerable shift towards values ≤1, which indicates a freely and/or subdiffusive motion (Fig. 6e, right). This supports the involvement of the microtubule network for droplet movement. In addition, the distribution of track straightness and root mean square velocity of the droplets weighted towards lower values both for 48 h and nocodazole-treated cells compared with those of the droplets at 24 h (Supplementary Fig. 15). Overall, these results suggest that movement of the liquid-like α-Syn droplets is initially much more directed with the assistance of the microtubules, which is substantially reduced upon liquid-to-solid transition and its localization to the perinuclear area.

Liquid-to-solid transition of α-Syn triggers aggresome formation. As α-Syn liquid droplets transformed into more rigid assemblies over time, we asked whether LLPS triggers α-Syn amyloid aggregation in cells. We probed the fibril formation using the amyloid-specific OC antibody[67] with immunoprecipitated α-Syn at different time points. A dot blot assay revealed that the OC signal increased for both treated and untreated cells over time (Fig. 6g and Supplementary Fig. 16). However, cells treated for 48 h showed a considerably increased OC immunoreactivity compared with that of untreated cells. Strikingly, the cell viability remained uncompromised (Supplementary Fig. 16), which could be due to the

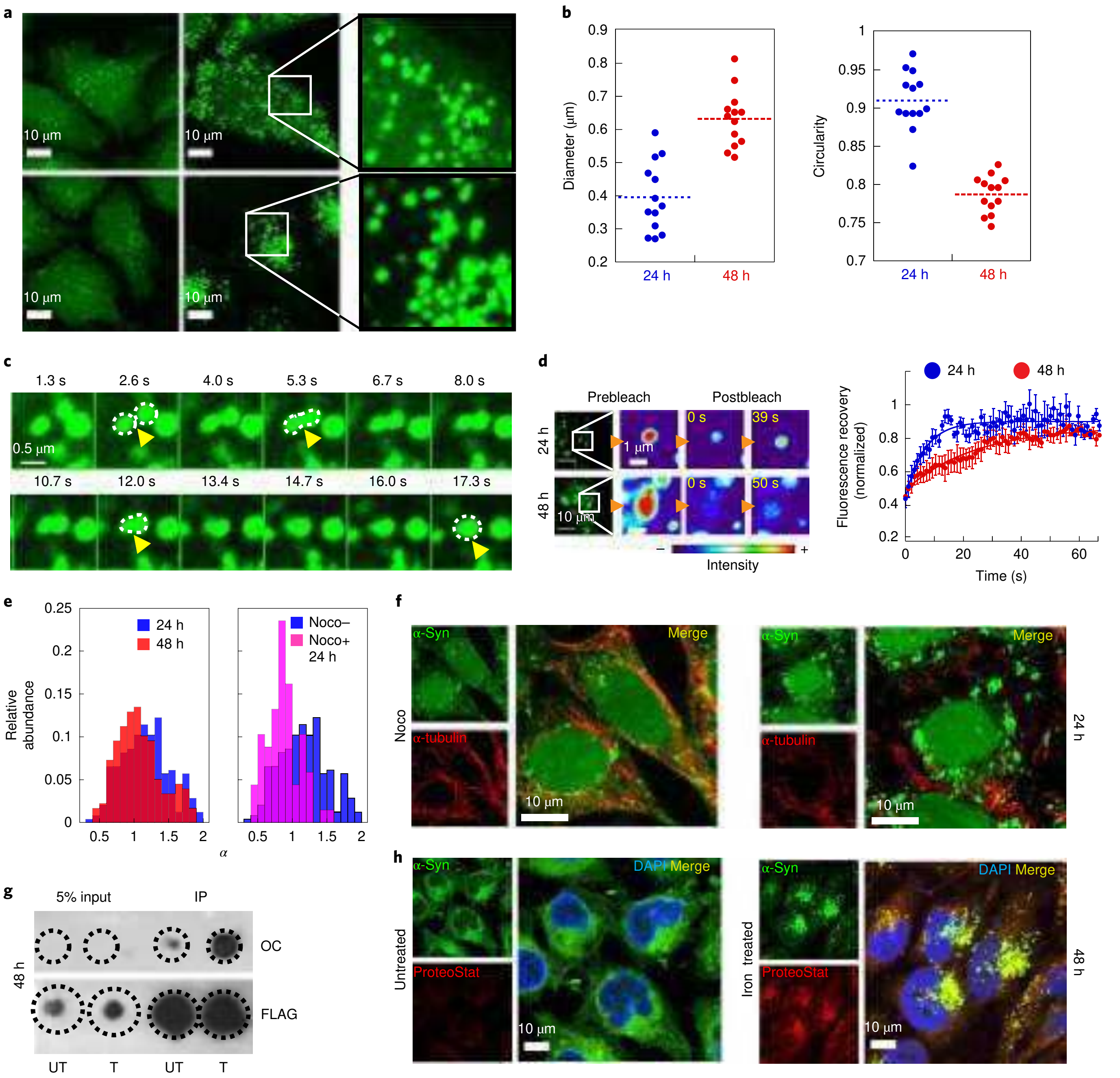

Fig. 6 | Liquid-like condensates of α-Syn in cells. a, Representative confocal images of HeLa cells overexpressing C4-α-Syn stained with FlAsH-EDT$_2$ captured at 24 h (top) and 48 h (bottom). Untreated cells (left) predominantly show pancellular localization; however, cells treated with 10 mM ammonium ferric citrate (right, ×10 magnification) show intracellular liquid-like droplet formation. The experiments were repeated independently five times with similar observations. **b**, Quantification of the diameter and circularity of droplets in iron-treated cells. The total number of droplets accounted is $n = 2,400$ (for 24 h) and $n = 950$ (for 48 h) from 13 independent microscopic fields. The dotted line (the measure of the centre) defines the mean of the values. **c**, The images represent a time-lapse series of the fusion event captured at 24 h after iron treatment. The experiments were repeated independently three times. **d**, In-cell FRAP recovery of droplets at 24 and 48 h of treatment. Left: the images correspond to the prebleach and postbleach droplets at $t = 0$ s and $t = 39$ s (24 h) and $t = 50$ s (48 h), represented in thermal pseudocolour. Right: normalized fluorescence recovery curves for 24 and 48 h droplets showing a slow recovery for the 48 h droplets compared with 24 h ones. The % recovery for the 24 and 48 h droplets were ~57% and ~36%, respectively. The data are shown as mean ± s.e.m. $n = 5$ independent experiments. Owing to the difference in the bleach region of interest, a diffusion constant could not be computed. **e**, Distribution plot of the diffusion exponent (α) calculated based on the log–log fit of the mean squared displacement versus time plot. The plots present a comparison of droplet behaviour after 24 and 48 h of iron treatment (left) and 24 h with and without treatment of nocodazole (noco) (right). **f**, Immunofluorescence images for α-tubulin staining of 24-h iron-treated HeLa cells with (right) or without (left) nocodazole. $n = 2$ independent experiments. **g**, Immunoprecipitation of α-Syn using anti-FLAG from cell extracts of the iron-treated and untreated cells after 48 h, and subsequent dot blots probed with amyloid-specific OC antibodies. Samples were probed with the FLAG antibody to ensure an equal loading of the immunoprecipitates (IPs). A 5% input of the total protein is also shown. UT, untreated; T, treated with iron. **h**, Aggresome detection using ProteoStat dye staining. After 48 h of treatment, α-Syn localized at the perinuclear region and showed colocalization with the ProteoStat dye, whereas the untreated cells showed no dye binding. All the experiments for **f–h** were repeated independently twice with similar results. DAPI, 4′,6-diamidino-2-phenylindole.

formation of perinuclear aggresomes[68]. Indeed, the aggresome formation in HeLa cells due to Fe^{3+} or Cu^{2+} treatment was confirmed by colocalization of α-Syn with ProteoStat (an aggresome marker) and the corresponding aggresome propensity factor (Fig. 6h and Extended Data Fig. 6). Overall, the data suggest metal-induced LLPS triggers aggresome formation in cells, which is regulated by microtubules.

Discussion

We showed that α-Syn phase separates and forms liquid droplets either in the presence of molecular crowding (PEG) or at a low pH (Fig. 1), the conditions that promote intermolecular interactions and/or an increase in the local concentration of α-Syn[69,70]. Initially, α-Syn droplets possessed liquid-like properties, as suggested by their physical shape, high diffusivity and temperature reversibility (Fig. 2). Interestingly, α-Syn possessed a significant amount of molecular rigidity inside the droplets immediately after formation as compared with that of outside (Fig. 2f,g). This suggests a distinct molecular signature of the proteins inside the droplets, irrespective of their liquid-like state. With time, these droplets became more rigid with fewer dynamic α-Syn molecules, consistent with a liquid-to-solid-like transition.

The direct implication of α-Syn LLPS in PD is apparent as PD-associated factors, which accelerate α-Syn aggregation, promote liquid-droplet formation and liquid-to-solid transitions (Fig. 3). In addition, conditions that retard α-Syn aggregation also delay or inhibit LLPS, which suggests that LLPS might be a critical step to nucleate its aggregation. Previous studies showed that a liquid-to-solid-like transition is associated with fibril formation by multiple proteins[10,22–24]; however, the direct demonstration of LLPS in the pathway(s) of aggregation has not been established. Amyloid aggregation generally occurs through a nucleation-dependent polymerization reaction with three distinct phases (lag, elongation and stationary)[71]. The parallel monitoring of LLPS and aggregation kinetics showed that liquid droplets first appeared at the early lag phase of α-Syn aggregation and fibrils were seen inside the droplets during the elongation phase. Intriguingly, α-Syn remains mostly in the monomeric state (LMW) during the early stages of LLPS, as weak intermolecular interactions by the protein govern the liquid-droplet formation[3,72]. However, over time, α-Syn gradually converts into oligomers and fibrils concurrently with the liquid-to-solid-like transition, which leads to a gel state (Fig. 4). In this context, our previous data suggest that α-Syn hydrogels could entrap cytotoxic α-Syn oligomers and fibrils[56], which indicates that LLPS and gel formation could be a toxic process associated with PD.

The intersection of α-Syn LLPS with previous reports becomes particularly important to understand the biochemical aspects of various proteins associated with aggregation and neurological disorders. Structural and functional differences in the proteins may govern the biophysical properties and fate of phase-separated droplets. For instance, the physiological role of FUS in stress granules requires the formation of reversible liquid droplets and hydrogel-like structures[21]. However, the disease-associated mutations induce an aberrant phase transition into an aggregate state, which is irreversible in nature[21,22]. Similarly, the LLPS of hnRNPA1 contributes to the assembly of stress granules and dysregulation of its inherent capability to cycle between the liquid and solid states results in an irreversible aggregated state[10]. Further, in the case of tau, no typical LCD exists, but still the protein exhibits a phase transition that leads to a disease-associated amyloid-like state[23]. By analogy, α-Syn at a high local concentration and in the presence of disease-associated conditions results in an aberrant phase transition that leads to its aggregation. Moreover, the LLPS of different proteins is known to be majorly driven by electrostatic interactions[23] and mediated through LCD domains[10,22]. In case of α-Syn, phase separation is mediated by an interplay of electrostatic interactions in the unstructured N-terminal domain and hydrophobic interactions in the NAC domain. During maturation, the C-terminus domain of α-Syn also becomes involved in the liquid-to-solid transition, which leads to amyloid aggregation (Fig. 5).

Previous reports show that a high local concentration, change in pH, temperature or specific ligand binding (such as RNA) induce protein LLPS in cells[16,19,73,74]. Our cellular studies showed that α-Syn in the presence of metal ions (iron or copper) forms liquid droplets (Fig. 6 and Extended Data Fig. 5). This metal-induced LLPS could be either due to a direct metal–α-Syn interaction that leads to structural changes and oligomerization[48,75,76] or to an oxidative stress (reactive oxygen species generation), which promotes α-Syn aggregation[77,78]. These liquid droplets convert to the solid-like state with the concomitant formation of amyloid-like aggregates (OC antibody positive). The maturation of these droplets eventually leads to aggresome formation, which is a cytoprotective mechanism against protein aggregates[68]. Interestingly, the dynamics of these droplets as well as their maturation into aggresome are assisted by microtubules. In this context, actin filaments are reported to influence the localization and/or movement of liquid condensates of the LAT (linker for activation of T cells) cluster[79,80] and provide mechanical support to the large nucleus of *Xenopus laevis* oocytes against gravitational forces[81].

Based on our observations, we propose a model for LLPS-mediated α-Syn aggregation (Supplementary Fig. 17). Under normal physiological conditions, α-Syn does not undergo LLPS, possibly due to its auto-inhibited conformational state, but at a high local concentration, due to pH changes, metal exposure, lipid interaction and mutation, the protein phase separates and forms liquid droplets. Slow maturation and ageing eventually convert the droplets into solid-like hydrogels composed of structurally ordered oligomers and amyloid fibrils. This process might be associated with cellular toxicity and the cell-to-cell transmission of amyloid[82] in neuronal cells associated with PD.

Online content

Any Nature Research reporting summaries, source data, extended data, supplementary information, acknowledgements, peer review information; details of author contributions and competing interests; and statements of data and code availability are available at https://doi.org/10.1038/s41557-020-0465-9.

Received: 10 May 2019; Accepted: 7 April 2020;
Published online: 8 June 2020

References

1. Brangwynne, C. P. et al. Germline P granules are liquid droplets that localize by controlled dissolution/condensation. *Science* **324**, 1729–1732 (2009).
2. Banani, S. F. et al. Compositional control of phase-separated cellular bodies. *Cell* **166**, 651–663 (2016).
3. Shin, Y. & Brangwynne, C. P. Liquid phase condensation in cell physiology and disease. *Science* **357**, eaaf4382 (2017).
4. Hyman, A. A., Weber, C. A. & Julicher, F. Liquid–liquid phase separation in biology. *Annu. Rev. Cell Dev. Biol.* **30**, 39–58 (2014).
5. Boeynaems, S. et al. Protein phase separation: a new phase in cell biology. *Trends Cell Biol.* **28**, 420–435 (2018).
6. Alberti, S. Phase separation in biology. *Curr. Biol.* **27**, R1097–R1102 (2017).
7. Holehouse, A. S. & Pappu, R. V. Functional implications of intracellular phase transitions. *Biochemistry* **57**, 2415–2423 (2018).
8. Feric, M. et al. Coexisting liquid phases underlie nucleolar subcompartments. *Cell* **165**, 1686–1697 (2016).
9. Kaiser, T. E., Intine, R. V. & Dundr, M. De novo formation of a subnuclear body. *Science* **322**, 1713–1717 (2008).
10. Molliex, A. et al. Phase separation by low complexity domains promotes stress granule assembly and drives pathological fibrillization. *Cell* **163**, 123–133 (2015).
11. Lin, Y., Protter, D. S., Rosen, M. K. & Parker, R. Formation and maturation of phase-separated liquid droplets by RNA-binding proteins. *Mol. Cell* **60**, 208–219 (2015).
12. Riback, J. A. et al. Stress-triggered phase separation is an adaptive, evolutionarily tuned response. *Cell* **168**, 1028–1040 (2017).

13. Brangwynne, C. P., Tompa, P. & Pappu, R. V. Polymer physics of intracellular phase transitions. *Nat. Phys.* **11**, 899–904 (2015).
14. Wei, M. T. et al. Phase behaviour of disordered proteins underlying low density and high permeability of liquid organelles. *Nat. Chem.* **9**, 1118–1125 (2017).
15. Hughes, M. P. et al. Atomic structures of low-complexity protein segments reveal kinked β sheets that assemble networks. *Science* **359**, 698–701 (2018).
16. Maharana, S. et al. RNA buffers the phase separation behavior of prion-like RNA binding proteins. *Science* **360**, 918–921 (2018).
17. Pak, C. W. et al. Sequence determinants of intracellular phase separation by complex coacervation of a disordered protein. *Mol. Cell* **63**, 72–85 (2016).
18. Burke, K. A., Janke, A. M., Rhine, C. L. & Fawzi, N. L. Residue-by-residue view of in vitro FUS granules that bind the C-terminal domain of RNA polymerase II. *Mol. Cell* **60**, 231–241 (2015).
19. Nott, T. J. et al. Phase transition of a disordered nuage protein generates environmentally responsive membraneless organelles. *Mol. Cell* **57**, 936–947 (2015).
20. Zhang, H. et al. RNA controls polyQ protein phase transitions. *Mol. Cell* **60**, 220–230 (2015).
21. Murakami, T. et al. ALS/FTD mutation-induced phase transition of FUS liquid droplets and reversible hydrogels into irreversible hydrogels impairs RNP granule function. *Neuron* **88**, 678–690 (2015).
22. Patel, A. et al. A liquid-to-solid phase transition of the ALS protein FUS accelerated by disease mutation. *Cell* **162**, 1066–1077 (2015).
23. Wegmann, S. et al. Tau protein liquid–liquid phase separation can initiate tau aggregation. *EMBO J.* **37**, e98049 (2018).
24. Conicella, A. E., Zerze, G. H., Mittal, J. & Fawzi, N. L. ALS mutations disrupt phase separation mediated by α-helical structure in the TDP-43 low-complexity C-terminal domain. *Structure* **24**, 1537–1549 (2016).
25. Ambadipudi, S., Biernat, J., Riedel, D., Mandelkow, E. & Zweckstetter, M. Liquid–liquid phase separation of the microtubule-binding repeats of the Alzheimer-related protein Tau. *Nat. Commun.* **8**, 275 (2017).
26. Burre, J. et al. Properties of native brain α-synuclein. *Nature* **498**, E4–E6 (2013).
27. Lashuel, H. A., Overk, C. R., Oueslati, A. & Masliah, E. The many faces of α-synuclein: from structure and toxicity to therapeutic target. *Nat. Rev. Neurosci.* **14**, 38–48 (2013).
28. Wong, Y. C. & Krainc, D. α-Synuclein toxicity in neurodegeneration: mechanism and therapeutic strategies. *Nat. Med.* **23**, 1–13 (2017).
29. Mehra, S., Sahay, S. & Maji, S. K. α-Synuclein misfolding and aggregation: implications in Parkinson's disease pathogenesis. *Biochim. Biophys. Acta Proteins Proteom.* **1867**, 890–908 (2019).
30. Polymeropoulos, M. H. et al. Mutation in the α-synuclein gene identified in families with Parkinson's disease. *Science* **276**, 2045–2047 (1997).
31. Zarranz, J. J. et al. The new mutation, E46K, of α-synuclein causes Parkinson and Lewy body dementia. *Ann. Neurol.* **55**, 164–173 (2004).
32. Flagmeier, P. et al. Mutations associated with familial Parkinson's disease alter the initiation and amplification steps of α-synuclein aggregation. *Proc. Natl Acad. Sci. USA* **113**, 10328–10333 (2016).
33. Cremades, N. et al. Direct observation of the interconversion of normal and toxic forms of α-synuclein. *Cell* **149**, 1048–1059 (2012).
34. Fusco, G. et al. Structural basis of membrane disruption and cellular toxicity by α-synuclein oligomers. *Science* **358**, 1440–1443 (2017).
35. Goedert, M., Jakes, R. & Spillantini, M. G. The synucleinopathies: twenty years on. *J. Parkinson. Dis.* **7**, S51–S69 (2017).
36. Spillantini, M. G. & Goedert, M. Neurodegeneration and the ordered assembly of α-synuclein. *Cell Tissue Res.* **373**, 137–148 (2018).
37. Giasson, B. I., Murray, I. V., Trojanowski, J. Q. & Lee, V. M. A hydrophobic stretch of 12 amino acid residues in the middle of α-synuclein is essential for filament assembly. *J. Biol. Chem.* **276**, 2380–2386 (2001).
38. Li, B. S. et al. Cryo-EM of full-length α-synuclein reveals fibril polymorphs with a common structural kernel. *Nat. Commun.* **9**, 3609 (2018).
39. Guerrero-Ferreira, R. et al. Cryo-EM structure of α-synuclein fibrils. *eLife* **7**, e36402 (2018).
40. Letunic, I. & Bork, P. 20 years of the SMART protein domain annotation resource. *Nucleic Acids Res.* **46**, D493–D496 (2018).
41. Meszaros, B., Erdos, G. & Dosztanyi, Z. IUPred2A: context-dependent prediction of protein disorder as a function of redox state and protein binding. *Nucleic Acids Res.* **46**, W329–W337 (2018).
42. Posey, A. E., Holehouse, A. S. & Pappu, R. V. Phase separation of intrinsically disordered proteins. *Methods Enzymol.* **611**, 1–30 (2018).
43. Voorhees, P. W. Ostwald ripening of two-phase mixtures. *Annu. Rev. Mater. Sci.* **22**, 197–215 (1992).
44. Berry, J., Weber, S. C., Vaidya, N., Haataja, M. & Brangwynne, C. P. RNA transcription modulates phase transition-driven nuclear body assembly. *Proc. Natl Acad. Sci. USA* **112**, E5237–E5245 (2015).
45. Smith, T. A. & Ghiggino, K. P. A review of the analysis of complex time-resolved fluorescence anisotropy data. *Methods Appl. Fluoresc.* **3**, 022001 (2015).
46. Lakowicz, J. R. *Principles of Fluorescence Spectroscopy* (Springer Science & Business Media, 2013).
47. Ghosh, D., Mehra, S., Sahay, S., Singh, P. K. & Maji, S. K. α-Synuclein aggregation and its modulation. *Int. J. Biol. Macromol.* **100**, 37–54 (2017).
48. Binolfi, A. et al. Interaction of α-synuclein with divalent metal ions reveals key differences: a link between structure, binding specificity and fibrillation enhancement. *J. Am. Chem. Soc.* **128**, 9893–9901 (2006).
49. Galvagnion, C. et al. Lipid vesicles trigger α-synuclein aggregation by stimulating primary nucleation. *Nat. Chem. Biol.* **11**, 229–234 (2015).
50. Samuel, F. et al. Effcts of serine 129 phosphorylation on α-synuclein aggregation, membrane association, and internalization. *J. Biol. Chem.* **291**, 4374–4385 (2016).
51. Breydo, L., Wu, J. W. & Uversky, V. N. α-Synuclein misfolding and Parkinson's disease. *Biochim. Biophys. Acta* **261–285**, 2012 (**1822**).
52. Conway, K. A., Rochet, J. C., Bieganski, R. M. & Lansbury, P. T. Jr. Kinetic stabilization of the α-synuclein protofibril by a dopamine-α-synuclein adduct. *Science* **294**, 1346–1349 (2001).
53. Rasia, R. M. et al. Structural characterization of copper(ii) binding to α-synuclein: insights into the bioinorganic chemistry of Parkinson's disease. *Proc. Natl Acad. Sci. USA* **102**, 4294–4299 (2005).
54. Abeyawardhane, D. L. et al. Copper induced radical dimerization of α-synuclein requires histidine. *J. Am. Chem. Soc.* **140**, 17086–17094 (2018).
55. Ghosh, D. et al. Structure based aggregation studies reveal the presence of helix-rich intermediate during α-synuclein aggregation. *Sci. Rep.* **5**, 9228 (2015).
56. Kumar, R. et al. Cytotoxic oligomers and fibrils trapped in a gel-like state of α-synuclein assemblies. *Angew. Chem. Int. Ed.* **57**, 5262–5266 (2018).
57. Winner, B. et al. In vivo demonstration that α-synuclein oligomers are toxic. *Proc. Natl Acad. Sci. USA* **108**, 4194–4199 (2011).
58. Endres, R. G. *Physical Principles in Sensing and Signaling: With an Introduction to Modeling in Biology* (Oxford Univ. Press, 2013).
59. Bartels, T., Choi, J. G. & Selkoe, D. J. α-Synuclein occurs physiologically as a helically folded tetramer that resists aggregation. *Nature* **477**, 107–110 (2011).
60. Sahay, S. et al. Familial Parkinson disease-associated mutations alter the site-specific microenvironment and dynamics of α-synuclein. *J. Biol. Chem.* **290**, 7804–7822 (2015).
61. Jha, S. K. & Udgaonkar, J. B. Direct evidence for a dry molten globule intermediate during the unfolding of a small protein. *Proc. Natl Acad. Sci. USA* **106**, 12289–12294 (2009).
62. Uversky, V. N. et al. Biophysical properties of the synucleins and their propensities to fibrillate: inhibition of α-synuclein assembly by β- and γ-synucleins. *J. Biol. Chem.* **277**, 11970–11978 (2002).
63. Vilar, M. et al. The fold of α-synuclein fibrils. *Proc. Natl Acad. Sci. USA* **105**, 8637–8642 (2008).
64. Sian-Hulsmann, J., Mandel, S., Youdim, M. B. & Riederer, P. The relevance of iron in the pathogenesis of Parkinson's disease. *J. Neurochem.* **118**, 939–957 (2011).
65. Matak, P. et al. Disrupted iron homeostasis causes dopaminergic neurodegeneration in mice. *Proc. Natl Acad. Sci. USA* **113**, 3428–3435 (2016).
66. Greenspan, P., Mayer, E. P. & Fowler, S. D. Nile red: a selective fluorescent stain for intracellular lipid droplets. *J. Cell Biol.* **100**, 965–973 (1985).
67. Kayed, R. et al. Fibril specific, conformation dependent antibodies recognize a generic epitope common to amyloid fibrils and fibrillar oligomers that is absent in prefibrillar oligomers. *Mol. Neurodegener.* **2**, 18 (2007).
68. Johnston, J. A., Ward, C. L. & Kopito, R. R. Aggresomes: a cellular response to misfolded proteins. *J. Cell Biol.* **143**, 1883–1898 (1998).
69. Shtilerman, M. D., Ding, T. T. & Lansbury, P. T. Jr. Molecular crowding accelerates fibrillization of α-synuclein: could an increase in the cytoplasmic protein concentration induce Parkinson's disease? *Biochemistry* **41**, 3855–3860 (2002).
70. Wu, K. P., Weinstock, D. S., Narayanan, C., Levy, R. M. & Baum, J. Structural reorganization of α-synuclein at low pH observed by NMR and REMD simulations. *J. Mol. Biol.* **391**, 784–796 (2009).
71. Wood, S. J. et al. α-Synuclein fibrillogenesis is nucleation-dependent—implications for the pathogenesis of Parkinson's disease. *J. Biol. Chem.* **274**, 19509–19512 (1999).
72. Banani, S. F., Lee, H. O., Hyman, A. A. & Rosen, M. K. Biomolecular condensates: organizers of cellular biochemistry. *Nat. Rev. Mol. Cell Biol.* **18**, 285–298 (2017).
73. Munder, M. C. et al. A pH-driven transition of the cytoplasm from a fluid to a solid-like state promotes entry into dormancy. *eLife* **5**, e09347 (2016).
74. Shin, Y. Spatiotemporal control of intracellular phase transitions using light-activated optodroplet. *Cell* **168**, 159–171 (2017).
75. Uversky, V. N., Li, J. & Fink, A. L. Metal-triggered structural transformations, aggregation, and fibrillation of human α-synuclein. A possible molecular NK between Parkinson's disease and heavy metal exposure. *J. Biol. Chem.* **276**, 44284–44296 (2001).
76. Abeyawardhane, D. L. et al. Iron redox chemistry promotes antiparallel oligomerization of α-synuclein. *J. Am. Chem. Soc.* **140**, 5028–5032 (2018).
77. Levin, J. et al. Generation of ferric iron links oxidative stress to α-synuclein oligomer formation. *J. Parkinson. Dis.* **1**, 205–216 (2011).

78. Chinta, S. J. & Andersen, J. K. Redox imbalance in Parkinson's disease. *Biochim. Biophys. Acta* **1780**, 1362–1367 (2008).
79. Kaizuka, Y., Douglass, A. D., Varma, R., Dustin, M. L. & Vale, R. D. Mechanisms for segregating T cell receptor and adhesion molecules during immunological synapse formation in Jurkat T cells. *Proc. Natl Acad. Sci. USA* **104**, 20296–20301 (2007).
80. Yi, J., Wu, X. S., Crites, T. & Hammer, J. A. 3rd Actin retrograde flow and actomyosin II arc contraction drive receptor cluster dynamics at the immunological synapse in Jurkat T cells. *Mol. Biol. Cell* **23**, 834–852 (2012).
81. Feric, M. & Brangwynne, C. P. A nuclear F-actin scaffold stabilizes ribonucleoprotein droplets against gravity in large cells. *Nat. Cell Biol.* **15**, 1253–1259 (2013).
82. Guo, J. L. & Lee, V. M. Cell-to-cell transmission of pathogenic proteins in neurodegenerative diseases. *Nat. Med.* **20**, 130–138 (2014).

Methods

Protein expression and purification was performed and in vitro LLPS was carried out using LMW α-Syn in the presence of various factors. The liquid droplets were visualized under an optical microscope. The dynamics of α-Syn during LLPS was studied using FRAP and microscopy-based time-resolved anisotropy decay measurements. α-Syn aggregation during LLPS was studied using ThT fluorescence and ThioS binding, and the structure and morphology of the aggregates and gels were analysed using TEM and SEM. The domain involvement of α-Syn during LLPS was studied using two-dimensional NMR, time-resolved lifetime and anisotropy decay and FRET analyses. LLPS in cells was carried out using HeLa cells overexpressing C4-tagged α-Syn. The liquid droplets in the cells were characterized using FRAP, single-particle tracking and other immunofluorescence methods for amyloid and aggresome detection. The detailed methods are provided in Supplementary Methods.

Reporting summary. Further information on research design is available in the Nature Research Reporting Summary linked to this article.

Data availability

The authors declare that all the data supporting the findings of this study are available within the article, in the source data files and in the Supplementary Information files. All the data analysis was performed using published tools and packages and has been provided with the paper.

Acknowledgements

We thank R. Mallik, S. Sen and M. Rao for critical inputs on the manuscript. We also acknowledge IIT Bombay Central Facilities for TEM, FACS and confocal microscopy to perform the experiments. We thank J. B. Udgaonkar for providing the TCSPC facility. We thank R. Reddy and S. Sen for their help in TCSPC microscopy experiments. We acknowledge C. Glabe for the kind gift of the OC antibody. The authors acknowledge DBT (BT/PR22749/BRB/10/1576/2016), Government of India for financial support, and N.S. acknowledges DST SERB (PDF/2016/003736) for funding.

Author contributions

S.R., R.K., K.P., J.M., R. Panigrahi, S. Mehra, L.G., D.C., A.S.S., S. Maiti and S.B. performed the in vitro and in silico experiments. N.S., S.P., D.D., A.N. and J.G. performed the in cell experiments. All authors participated in analysing the data. S.R. and N.S. contributed equally to this work. The study was conceived by S.K.M. and designed by S.K.M., G.K., R. Padinhateeri, A.K., A.C. and R.R. All authors participated in manuscript writing and approved the manuscript.

Competing interests

The authors declare no competing interests.

Additional information

Extended data is available for this paper at https://doi.org/10.1038/s41557-020-0465-9.

Supplementary information is available for this paper at https://doi.org/10.1038/s41557-020-0465-9.

Correspondence and requests for materials should be addressed to S.K.M.